ACS APPLIED MATERIALS & INTERFACES

www.acsami.org

Research Article

In/Ce Co-doped Li_3VO_4 and Nitrogen-modified Carbon Nanofiber Composites as Advanced Anode Materials for Lithium-ion Batteries

Yuanlang Wan, Zhi Chang, Xuefang Xie, Jialin Li, Simin Chai, Shuang Zhou, Qiong He, Chunyan Fu, Mingyang Feng, Guozhong Cao, Shuquan Liang, and Anqiang Pan*

Cite This: *ACS Appl. Mater. Interfaces* 2022, 14, 52702–52714

Read Online

ACCESS | Metrics & More | Article Recommendations | Supporting Information

ABSTRACT: Li_3VO_4 (LVO) is considered as a novel alternative anode material for lithium-ion batteries (LIBs) due to its high capacity and good safety. However, the inferior electronic conductivity impedes its further application. Here, nanofibers (*n*LICVO/NC) with In/Ce co-doped Li_3VO_4 strengthened by nitrogen-modified carbon are prepared. Density functional theory calculations demonstrate that In/Ce co-doping can substantially reduce the LVO band gap and achieve orders of magnitude increase (from 2.79 × 10^{-4} to 1.38 × 10^{-2} S cm^{-1}) in the electronic conductivity of LVO. Moreover, the carbon-based nanofibers incorporated with 5LICVO nanoparticles can not only buffer the structural strain but also form a good framework for electron transport. This 5LICVO/NC material delivers high reversible capacities of 386.3 and 277.9 mA h g^{-1} at 0.1 and 5 A g^{-1}, respectively. Furthermore, high discharge capacities of 335 and 259.5 mA h g^{-1} can be retained after 1200 and 4000 cycles at 0.5 and 1.6 A g^{-1}, respectively (with the corresponding capacity retention of 98.4 and 78.7%, respectively). When the 5LICVO/NC anode assembles with commercial $LiNi_{1/3}Co_{1/3}Mn_{1/3}O_2$ (NCM111) into a full cell, a high discharge capacity of 191.9 mA h g^{-1} can be retained after 600 cycles at 1 A g^{-1}, implying an inspiring potential for practical application in high-efficiency LIBs.

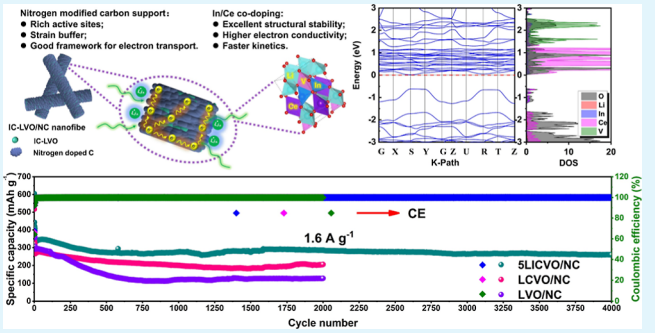

KEYWORDS: *Li_3VO_4, In/Ce co-doping, DFT, electronic conductivity, lithium-ion batteries*

1. INTRODUCTION

The continuous proliferation of electric vehicles, drones, and smartphones has put forward higher requirements for the energy density, power density, and cycle life of lithium-ion batteries (LIBs).[1−4] Suitable anode materials are the key to the development and application of novel LIBs. Presently, graphite and $Li_4Ti_5O_{12}$ (LTO) still dominate the market of anode materials for LIBs. However, the theoretical capacity of graphite (372 mA h g^{-1}) is low, and the working potential is close to 0 V versus Li^+/Li, which easily induce the formation of lithium dendrites and raise catastrophic battery safety issues. The spinel LTO, on the other hand, as a typical "zero-strain" material, possesses a low theoretical capacity (152 mA h g^{-1}), which greatly limits the energy density and power density of the batteries. Li_3VO_4 (LVO) based on the intercalation/extraction mechanism was first reported in 2013 and triggered widespread attention to be used as a potential anode material for LIBs.[5] LVO belongs to the orthorhombic system with a space group of $Pnm2_1$. Its crystal structure is composed of tetrahedra of LiO_4 and VO_4 connected by shared angles. The cations occupy the positions of ordered tetrahedra, while octahedra are vacant and connected to each other, forming a tunnel-type structure that can facilitate the diffusion of Li^+.[6] The prominent advantages of LVO involve high theoretical capacity (394 mA h g^{-1}, higher than that of graphite and LTO),[7−9] much safer platform voltage (~1 V vs Li^+/Li, higher than that of graphite but lower than that of LTO, which can effectively avoid the formation of lithium dendrites), high ionic conductivity (10^{-4} to 10^{-6} S cm^{-1}), small volume expansion (~4% when discharged to 0.7 V),[10] and easy and cheap to be manufactured. Hence, LVO is considered as a novel alternative material for the next generation of high energy and high power density LIB anodes.

Unfortunately, with the wide band gap, LVO is virtually an electronic insulator (the electronic conductivity is less than 10^{-10} S cm^{-1}), which leads to large resistance polarization and dramatically damages its rate performance.[11] Structural design (nanosphere,[12] microcubic structure,[13] honeycomb nanoclusters,[14] nanorods,[15] nanowires,[16,17] etc.) and composites with conductive materials (N-doped graphite,[18,19] porous carbon,[20−22] carbon nanotubes,[23] MXene,[24] Ni or NiO,[25,26]

Received: June 13, 2022
Accepted: August 12, 2022
Published: November 17, 2022

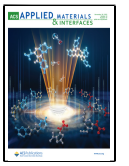

Scheme 1. Synthesis of In/Ce Co-doped Li_3VO_4 and N-doped Carbon (IC-LVO/NC) Nanofibers

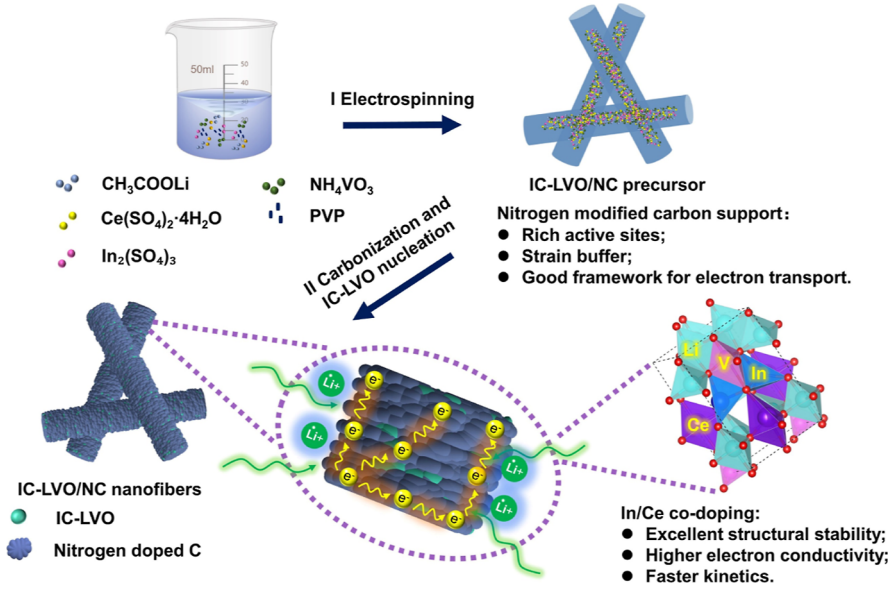

etc.) are effective methods to enhance the electrochemical performance of LVO. However, designing materials with hollow nanostructures (such as nanospheres and nanorods) frequently decreases the tap density of materials and results in the loss of the battery volume energy density, which is unfavorable for their practical applications. A tight structure incorporated with primary nanoparticles may be a better choice.[27] Meanwhile, structural design and making composites with conductive materials cannot improve the intrinsic electronic conductivity of LVO considerably,[28] and giant polarization of the battery seriously deteriorates the rate performance.

Ion doping is an effective method to promote a stable bulk phase structure, directly change the band gap, and effectively increase the intrinsic electronic conductivity of LVO.[29−31] For example, Liang et al. synthesized Cr and Si co-doped γ-crystalline LVO nanowires (γ-LCSVO-NW) via electrospinning (if not specified, the usual term LVO refers to β-crystalline).[32] The Cr^{3+} and Si^{4+} partially replaced V^{5+}, which notably enhanced the rate and cycling performance of LVO. Huu et al. synthesized 3% Ca^{2+}-doped LVO (3LCVO-ABR) based on an acid−base reaction (ABR).[33] Theoretical calculations show that Ca^{2+} as a doping modifier combined with the reaction characteristics of the ABR can provoke the formation of materials with mesoporous structures on their surface. Meanwhile, Ca^{2+} directly provides electrons for the reduction of V^{5+} to V^{4+} and significantly improves the electrode capacitive contribution with a high capacity of 477.1 mAg^{-1} when 3LCVO-ABR is used as an anode material for LIBs. In addition, Cu^{2+},[34] Ni^{2+},[35] Mg^{2+},[36] Nb^{2+},[11] Ti^{4+},[37] and other ions have also been applied to modify LVO, illustrating that ion doping is an effective method to improve the intrinsic electronic conductivity of LVO. Rare earth elements usually possess a high charge state, large radius, and low self-polarization. Nevertheless, there are still a few studies on doping modification of LVO with rare earth elements. Indium is also a superb dopant modifier and has an important role in defect and energy level structure modulation of electrode materials.[38,39]

Herein, considering the unique effects of rare earth elements and indium, nitrogen-modified carbon-supported In/Ce co-doped LVO (nLICVO/NC, n = 3, 5, 7, represents the molar ratios of In^{3+}/Ce^{4+}, where the molar amount of Ce^{4+} was fixed) were investigated to acquire a high-performance LIB material with high tap density. The conductive nanofibers (5LICVO/NC, sample with the best performance) tightly incorporated by 5LICVO nanoparticles were synthesized via electrospinning with subsequent one-step carbonization. The In/Ce co-doped LVO nanoparticles embedded in a N-modified highly amorphous carbon matrix of the nanofibers are obtained. The nanoparticles can enable the complete infiltration of the electrolyte, while the unique carbon nanofiber framework can buffer the strain and guarantee rapid electron transport. Density functional theory (DFT) calculations reveal that the LVO band gap is substantially reduced, and the carrier transport capacity is improved with the synergistic effect of In/Ce, which can significantly improve the Li^+ diffusion coefficient and electronic conductivity of the LVO material. With these merits, 5LICVO/NC exhibits superior rate and long-term cycling performance. When the 5LICVO/NC anode assembles with commercial $LiNi_{1/3}Co_{1/3}Mn_{1/3}O_2$ (NCM111) into a full cell, a high discharge capacity of 190.9 mA h g^{-1} can be retained after 600 cycles at 1 A g^{-1}, implying an inspiring potential for practical application in high-efficiency LIBs.

2. RESULTS AND DISCUSSION

2.1. Crystal Structure and Morphology. Scheme 1 illustrates the synthesis process of LICVO/NC nanofibers. In the process of stirring and electrospinning, the lithium source (CH_3COOLi), vanadium source (NH_4VO_3), indium source ($In_2(SO_4)_3$), and cerium source ($Ce(SO_4)_2·4H_2O$) can be dispersed in a continuous and uniform carbon precursor matrix, thereby alleviating drastic volume changes and inhibiting particle agglomeration. In the subsequent carbonization process, the PVP-derived nitrogen-doped carbon and the nucleation of LICVO occurred simultaneously, forming a compact hybrid structure/composite between LICVO and carbon on the nanoscale. The integration of LICVO crystals led to the formation of a carbon framework on the aggregates,

https://doi.org/10.1021/acsami.2c10471
ACS Appl. Mater. Interfaces 2022, 14, 52702−52714

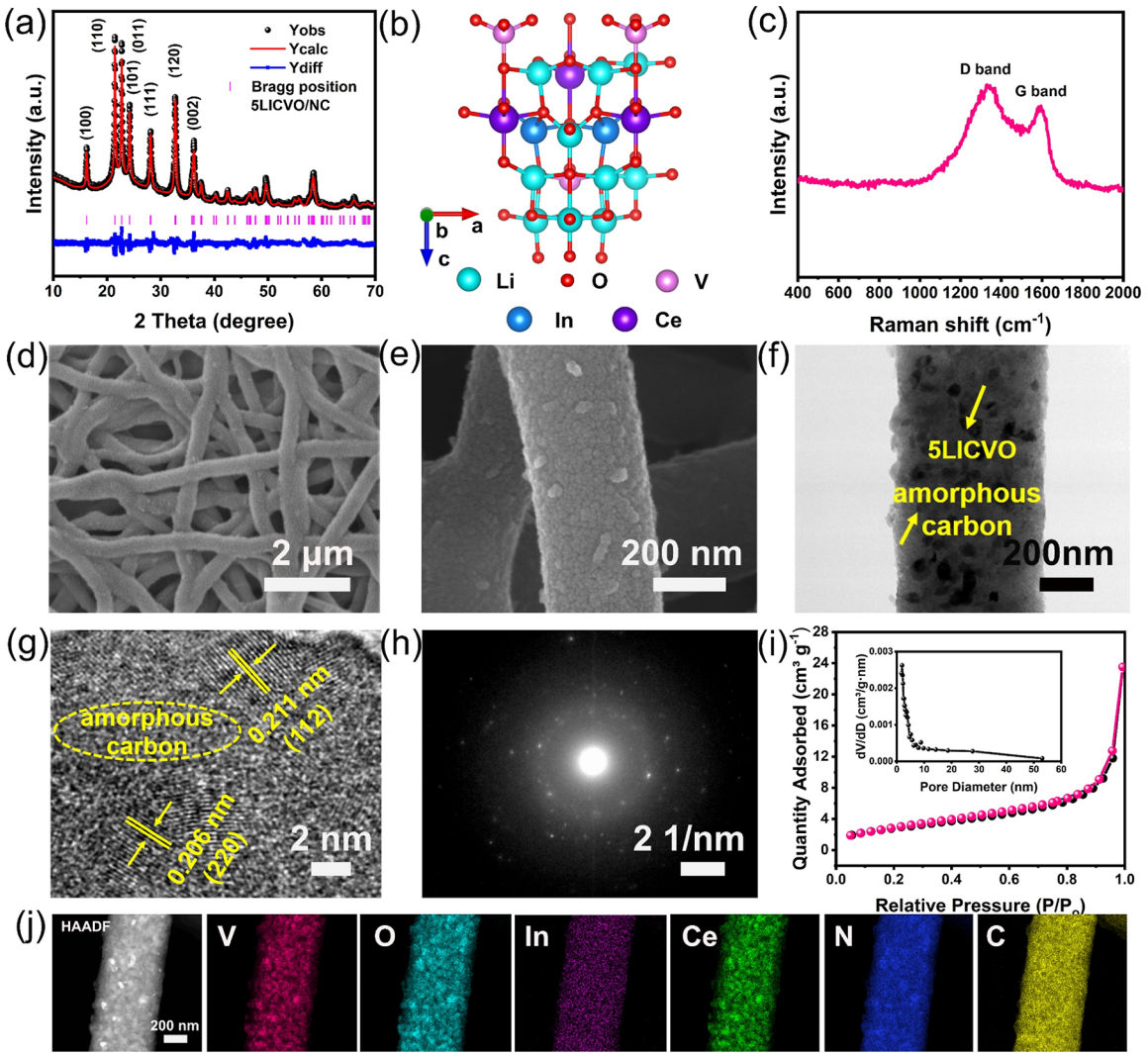

Figure 1. (a) Rietveld refined XRD spectrum, (b) crystal structure, (c) Raman spectrum, (d,e) field emission (FESEM), (f) TEM, (g) HRTEM, (h) SAED, (i) N_2 adsorption−desorption isotherm curves (inset for pore size distribution), and (j) HAADF and the elemental mapping images of 5LICVO/NC.

sustaining the fiber morphology of the precursor[40] (Figure S1). The formation of the carbon layer suppressed the growth of LICVO grains, shortened the diffusion path of Li^+, and maintained high electrochemical activity. Moreover, the In/Ce co-doping can improve the structural stability and electronic conductivity of LVO. Based on the above-mentioned merits, the LICVO and carbon nanofibers exhibit good rate capability and cycling stability.

The X-ray diffraction (XRD) spectra of the samples obtained by the co-doping of In^{3+}/Ce^{4+} with different molar ratios are shown in Figure S2. When the molar ratio of In^{3+}/Ce^{4+} was 5:1, the doped LVO product (5LICVO/NC) without noticeable impurities, while the impurity phase of $Li_2V_{1.16}O_2$ (PDF #76-2448) situated at around 44.44°, appeared in both 3LICVO/NC and 7LICVO/NC. Moreover, the excessive In^{3+} source reduction during the high-temperature carbonization process resulted in an impurity phase of In (PDF #85-1409) in 7LICVO/NC. Excellent rate performance generally indicates higher ionic and electronic conductivity of the samples. Hence, to further ascertain the optimal doping ratio, the rate performance of all composite samples was compared [Figures S3 and 4d (it will be further discussed in the following contents)]. The results reveal that 5LICVO/NC has the best rate performance, and a doping molar ratio of 5:1 for In^{3+}/Ce^{4+} is the best choice.

The XRD diffraction spectra of 5LICVO/NC (Figure 1a), LCVO/NC (Figure S4a), and LVO/NC (Figure S4b) were Rietveld refined by using the GSAS software with the EXPGUI interface. The calculated results of all samples are in good agreement with the experimental results. For 5LICVO/NC, LCVO/NC, and LVO/NC, the diffraction peaks located at 16.22, 21.44, 22.72, 24.22, 28.1, 32.68, and 36.18° correspond to the (100), (110), (011), (101), (111), (120), and (002) planes of Li_3VO_4(PDF card No. 38-1247), respectively, with orthorhombic and space group of $Pnm2_1$. There is no other impurity phase in 5LICVO/NC, which indicates the successful doping of the two ions. In and Ce prefer to occupy the V-site in the LVO tetrahedra (Figure 1b), and the ionic radius of In^{3+} (0.80 Å) and Ce^{4+} (0.87 Å) are larger than that of V^{5+} (0.54 Å) which leads to the expansion of the unit-cell volume after doping. A larger unit-cell volume can provide more space for the diffusion of Li^+ and facilitate the reduction of polarization.[28,29] The detailed 5LICVO/NC fractional atomic parameters and the relevant lattice parameters of three samples

https://doi.org/10.1021/acsami.2c10471
ACS Appl. Mater. Interfaces 2022, 14, 52702−52714

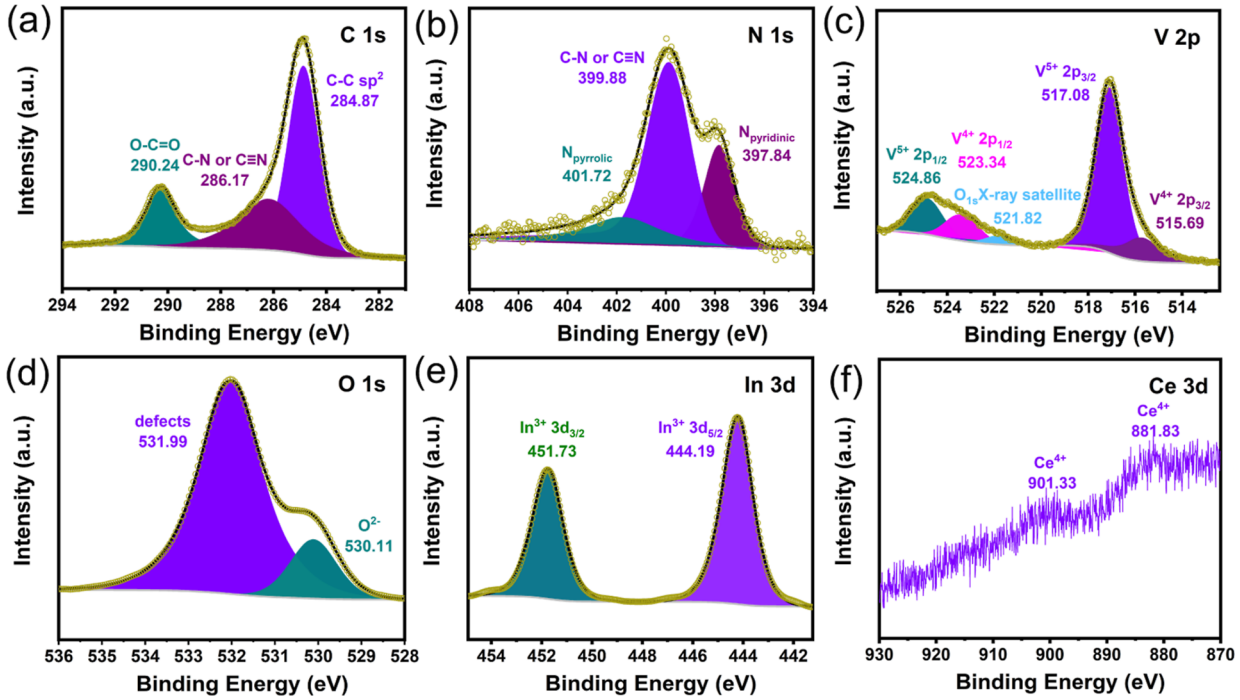

Figure 2. High-resolution XPS spectra of (a) C 1s, (b) N 1s, (c) V 2p, (d) O 1s, (e) In 3d, and (f) Ce 3d of 5LICVO/NC.

are shown in Tables S1 and S2. The small weighted profile error factors (R_{WP}) suggest the rationality of the In/Ce co-doping in this work.

The Raman spectrum of 5LICVO/NC (Figure 1c) shows two peaks situated at 1330 and 1593 cm^{-1}, reflecting the D-band of lattice defects and the G-band of stretching vibrations in the sp^2 hybridization plane of graphitic carbon,[41,42] respectively (I_D/I_G = 1.13 indicates the highly amorphous state of the carbon layer). 5LICVO/NC consists of carbon-based nanofibers with a lateral size of about 400 nm, and each fiber is entirely composed of a tightly packed irregular nanoparticles of 8−40 nm in diameter (Figure 1d,e) which ensures the good infiltration of the electrolyte. The tightly packed fibers with nanoparticles provided a high tap density and constructed a conductive framework for rapid electron transport. The carbon layer can suppress the grain growth of 5LICVO, shorten the path of Li^+ diffusion, improve the reaction kinetics, and buffer the structural strain during Li^+ intercalation/extraction of 5LICVO/NC. The scanning electron microscopy (SEM) images of 5LICVO/NC (Figure 1e), LCVO/NC (Figure S5a), and LVO/NC (Figure S5d) are compared. It can be found that 5LICVO/NC along with LCVO/NC are all composed of smaller LVO particles that are uniformly distributed on the carbon matrix than that of LVO/NC, which is more favorable for electrode reactions. The transmission electron microscopy (TEM) image (Figure 1f) shows that 5LICVO nanoparticles are randomly distributed in the amorphous carbon layer. The high resolution TEM (HRTEM) image (Figure 1g) shows clear lattice fringes with *d*-spacings of 0.211 and 0.206 nm, corresponding to the (112) and (220) planes of orthorhombic Li_3VO_4, respectively. Moreover, the amorphous regions respond to the distribution of amorphous carbon. A "built-in electric field" is formed at the interface between amorphous and crystalline state carbon, which can promote the rapid diffusion of Li^+.[43] The irregular diffraction spots and inconspicuous diffraction rings in the selected area electron diffraction (SAED) (Figure 1h) further imply that 5LICVO nanoparticles are randomly distributed in the amorphous carbon layer on the nanoscale. This also indicates that the low crystallinity of the amorphous carbon layer can suppress the grain growth.[17,40] The carbon content of 5LICVO/NC is about 38.40% (Figure S6), which corresponds to a BET specific surface area of 10.46 $m^2\ g^{-1}$ and an average pore size of 8.59 nm (Figure 1i). The high-angle annular dark-field image (HAADF) of 5LICVO/NC and the corresponding elemental mapping image (Figure 1j) further verify the successful doping of In/Ce. The elemental mapping suggests that C and N are uniformly distributed throughout the nanofiber, while V, O, In, and Ce display slight bias aggregation on the nanoscale, consisting of the above-mentioned morphology of 5LICVO/NC. It should be noted that N was derived from the decomposition of PVP at high temperatures,[17] which will be further discussed in the following contents.

The elemental valence states on the material surface were studied by X-ray photoelectron spectroscopy (XPS). The C 1s spectrum of 5LICVO/NC in Figure 2a can be deconvoluted into three peaks located at 284.87, 286.17, and 290.24 eV, which can be assigned to the C−C sp^2 hybrid orbital, C−N or C≡N, and O−C=O bonds,[44,45] respectively. This demonstrates the presence of nitrogen and oxygen-containing functional groups in the surface carbon layer, implying the presence of N-doped carbon.[46,47] This conclusion can be further confirmed through the high-resolution spectrum of N 1s. The three peaks located at 397.84, 399.88, and 401.72 eV in Figure 2b can be ascribed to the spin−orbit levels of pyridinic N, C−N or C≡N, and pyrrolic N, respectively, further demonstrating the successful preparation of N-doped carbon.[21,48] N doping can modify the carbon matrix to generate extrinsic defects in the amorphous carbon layer, which will act as active reaction sites and enhance the electrode reaction kinetics.[49] On the other hand, N-doped carbon is favorable for

https://doi.org/10.1021/acsami.2c10471
ACS Appl. Mater. Interfaces 2022, 14, 52702−52714

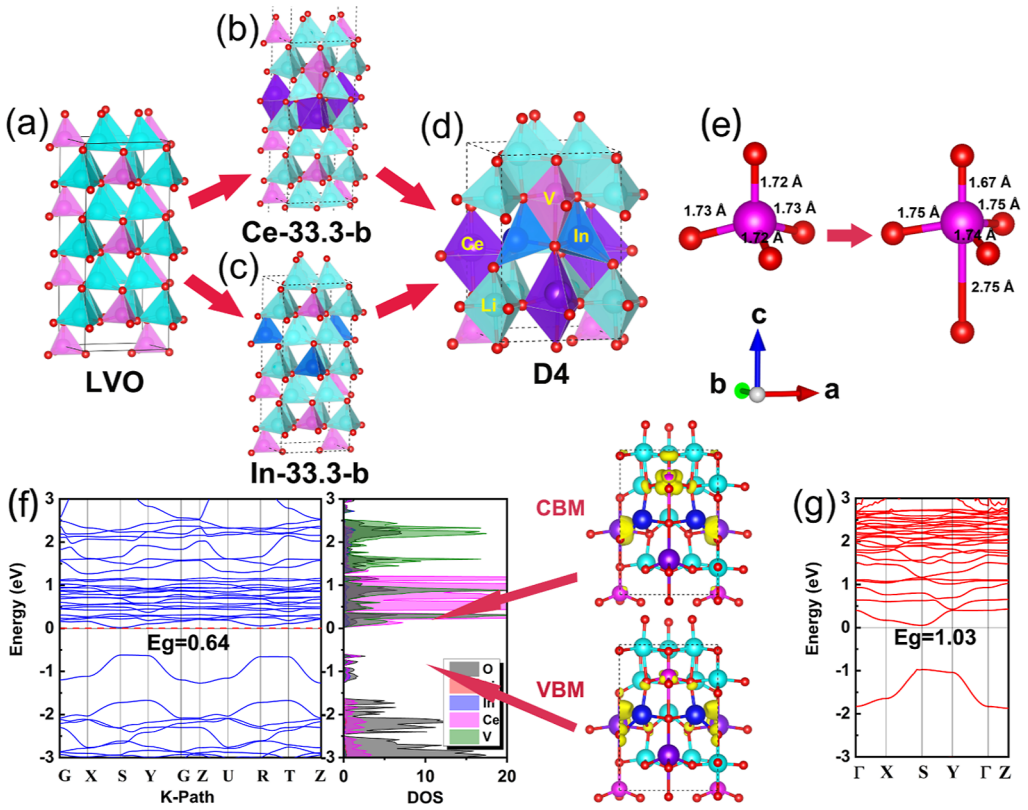

Figure 3. Crystal structures of (a) LVO, (b) Ce-33.3-b, (c) In-33.3-b, and (d) D4. (e) Schematic illustration of bond lengths (LVO on the left and Ce-33.3-b on the right). (f) Calculated energy band structure (blue based on PBE method), DOS and charge density diagrams of the conduction band edge (CBM) and valence band edge (VBM) and (g) calculated energy band structure of D4 based on the HSE method.

the formation of the fixed-domain sender level close to the Fermi level, which can increase the Fermi-surface density and improve the electronic conductivity.[50]

Figures 2c, S7c, and S9c represent the V 2p high-resolution spectra corresponding to 5LICVO/NC, LCVO/NC, and LVO/NC, respectively. The peak deconvolution of three samples of V 2p is similar. It can be found from Figure 2c that V 2p can be deconvoluted into five peaks. 521.82 eV is an O satellite peak, and the two peaks located at 517.08 and 524.86 eV reflect the spin−orbit levels of V $2P_{3/2}$ and V $2P_{1/2}$, respectively, indicating the presence of V^{5+}. The two peaks located at 515.69 and 523.34 eV indicate the presence of V^{4+} in the 5LICVO/NC.[51,52] It is worth noting that the V^{4+}/V^{5+} hybrids are present in all samples from the XPS analysis. However, the convolution ratio of V^{4+}/V^{5+} in 5LICVO/NC is 0.92, which is 1.02 times higher than that of LCVO/NC and 1.08 times higher than that of LVO/NC. This result illustrates that V^{4+} increases with more Ce^{4+} doping, while the introduction of In^{3+} combines with Ce^{4+} to provide electrons for the reduction of V^{5+} to V^{4+}, promoting the generation of more V^{4+}. V^{4+} in LVO/NC is caused by the reducing atmosphere during the high-temperature carbonization process. The V^{4+}/V^{5+} hybrids play an important role in improving the electrochemical performance of 5LICVO/NC. First, the partial loss of V^{5+} can cause the disappearance of the associated VO_4 tetrahedra in the LVO structure, thus extending the diffusion space of Li^+.[43] Second, V^{4+}/V^{5+} hybrids can regulate the LVO energy level structure, and the unpaired $3d^1$ electrons in V^{4+} are easily transported into the bulk phase lattice, which may lead to a smaller band gap and improve the electronic conductivity.[43] In addition, in order to maintain charge balance, the presence of V^{4+} means that O^{2-} in the system loses electrons and form O_2, followed by the release from the lattice ($V^{5+} + e^- \rightarrow V^{4+}$, $1/2O^{2-} - e^- \rightarrow 1/2O_2\uparrow$),[43] resulting in the generation of oxygen defects, as shown in the O 1s spectrum (Figure 2d). In the high-resolution spectrum of O1s, the two peaks located at 530.11 and 531.99 eV can be ascribed to O^{2-} and oxygen defects.[53,54] The oxygen defects combined with the extrinsic defects derived from N-modified carbon provide more active sites for enhancing the adsorption of cations, promoting rapid ion and electron transportation and producing a significant capacitive effect.[35,54] The two peaks at 444.19 and 451.73 eV in the high-resolution spectrum of In 3d (Figure 2e) can be assigned to the spin−orbit levels of In $3d_{5/2}$ and In $3d_{3/2}$, respectively, indicating the presence of In^{3+}.[55,56] The XPS high-resolution spectrum of Ce 3d in Figure 2f displays two peaks at 881.83 and 901.33 eV, indicating the presence of Ce^{4+}.[57−59]

2.2. Electronic Properties of In/Ce Co-doping. To clarify the effect of In/Ce co-doping on the electronic properties of LVO, DFT was used to calculate the band structure and density of states (DOS) of LVO using the Vienna ab initio simulation package. The LVO was subjected to substitutional doping of Ce and In on V atoms. The LVO structure of the 1 × 1 × 3 superlattice was chosen for the substitution doping of V atoms at different concentrations for the sake of computational rationality. The doping formation energy (E_f) was used to assess the thermodynamic stability of the system after doping, and according to eq S1, a negative value of the formation energy indicates that the system is exothermic after doping, and the structure is stable.

https://doi.org/10.1021/acsami.2c10471
ACS Appl. Mater. Interfaces 2022, 14, 52702−52714

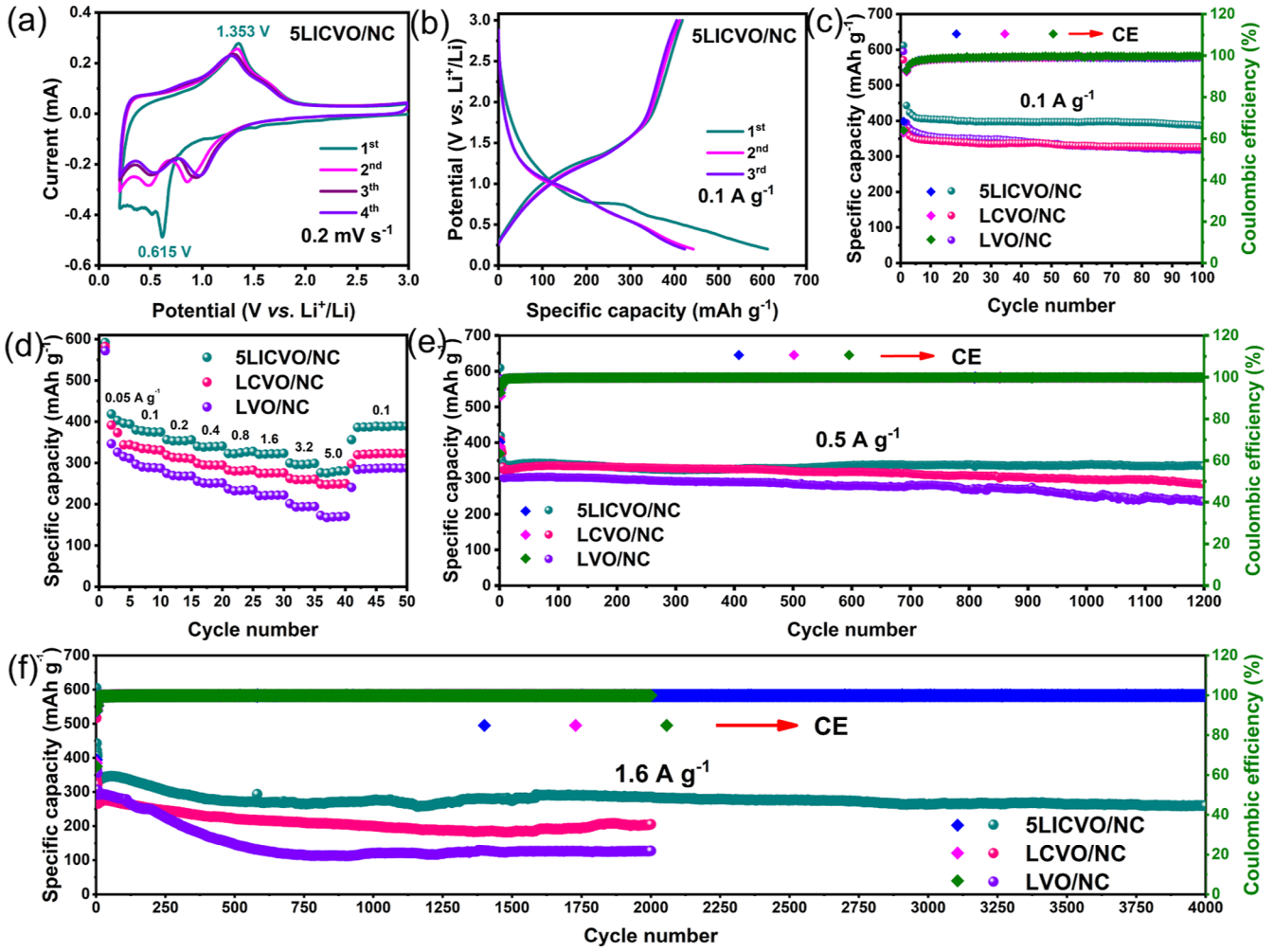

Figure 4. (a) CV curves for the first four cycles at 0.2 mV s^{-1} and (b) discharge/charge curves for the first three cycles at 0.1 A g^{-1} of 5LICVO/NC. (c) Cycling performance at 0.1 A g^{-1}, (d) rate performance, and (e,f) long-term cycling performance of three samples.

To understand the reasonable doping position and the effect of the doping concentration on the electronic properties (band gap) of the structure, Ce or In was used to replace the V atom. Initially, the mono-doping of LVO with Ce or In atoms was carried out separately. While replacing V atoms with Ce doping, the doping concentrations are 16.7, 33.3, and 50%, respectively, wherein 33.3% doping concentration consists of three different positions of doping sites (labeled a, b, and c). The doping models are denoted as Ce-16.7, Ce-33.3-a, Ce-33.3-b, Ce-33.3-c, and Ce-50, respectively (Figure S10). The doping formation energy of the system steadily becomes larger with increasing doping concentrations (Table S3), demonstrating that the structure becomes unstable with increasing doping concentrations. For example, the energy gap and dopant formation energy of the Ce-16.7 structure are 2.05 and −1.03 eV, respectively, while those of the Ce-50 structure are 2.27 and 2.06 eV, respectively. At 33.3% doping concentration, the dopant formation energy of the system is −0.72 eV, and the energy gap is 1.84 eV (only in the case of doping site b). Thus, the doping that can be performed with a diminished band gap is 33.3% doping of Ce at the b site, theoretically. In Ce-33.3-b, the VO tetrahedra will shift to VO octahedra (Figure 3b). When the VO tetrahedra are undoped, the V−O bond lengths are 1.72, 1.72, 1.73, and 1.73 Å, respectively. After the VO tetrahedra are distorted into VO octahedra, the V−O bond lengths are 1.67, 1.75, 1.74, 1.75, and 2.75 Å, respectively (Figure 3e), matching well with the XRD Rietveld refinement analysis. Then, the V atoms were substituted by In doping: with doping concentrations of 16.7, 33.3, and 50%, similarly denoted as In-16.7, In-33.3-a, In-33.3-b, In33.3-c, and In-50, respectively (Figure S11). The results demonstrated that the doping of In has a restricted effect on altering the energy gap toward this structure, and the system is stable at 33.3% doping concentration. In-33.3-b is doped in the same way as Ce-33.3-b; even though there is no VO tetrahedral distortion in In-33.3-b (Figure 3c), the energy gap of this structure is still the smallest among the In single-doped structures (Table S3). Consequently, we paid extra attention to the way of Ce-33.3-b substitution doping.

Under the premise of computational rationality, the binary substitution doping of the 1 × 1 × 2 superlattice of LVO to V was carried out following the 33.3%-b-Ce substitution doping method. After the optimization of the doped structure, both the PBE method and a much more accurate HSE06 method were employed to calculate the energy bands and DOS of the system to make the theoretical calculations closer to the actual values. The PBE method underestimates the band gap, and the HSE method calculates the band gap much in line with the actual values, as reported in previous studies.[60,61] PBE and HSE are basically the same in terms of the energy band

https://doi.org/10.1021/acsami.2c10471
ACS Appl. Mater. Interfaces 2022, 14, 52702−52714

structure profile and energy band curvature, except for the difference in the calculated energy gap values.

For In/Ce binary doping, seven types of doping were designed (Figure S13), and all of them were found to have VO tetrahedral distortion to VO octahedra in the structure, so the energy gap of the LVO binary doped structure was broadly reduced (Table S4). In the D4 doping type (Figure 3d), the system has the lowest energy gap value which is 0.64 eV (1.03 eV), calculated by the PBE (HSE06) method, matching well with the energy gap results obtained from UV−vis−NIR tests (Figure S14). In its energy band structure, the conduction band can be discovered closer to the Fermi energy level. From the DOS (Figure 3f), it can be revealed that the conduction band minimum (CBM) position consists of electrons from Ce and V, while the valence band maximum position (VBM) consists of holes from O and In. The same result is obtained from the energy band edge charge density diagram (Figure 3f), where the electrons are localized in the V and Ce atoms and the holes are localized in the O and In atoms (the calculated energy band structures, DOS plots), and band edge charge density plots for the remaining six structures are shown in the Figure S15. At the CBM position, the V atom gains electrons, implying that there is a change flow from V^{5+} to V^{4+}, which is in agreement with the results of the XPS analysis. To further examine whether the In/Ce binary doping is beneficial for improving the electron or hole mobility, a simple and effective way to qualitatively evaluate the carrier transport ability based on the effective mass of the band edge in the energy band structure is carried out. The effective masses in both D1 and D4 types are smaller than those in the other types (Table S4), indicating a relatively strong carrier transport capacity.

In a quantitative and qualitative sense, DFT calculations revealed that the introduction of Ce atoms in LVO can induce the transformation of VO tetrahedra into VO octahedra. On the other hand, the introduction of In atoms can serve to stabilize the structure and reduce the doping formation energy of the system. Therefore, the binary doping of Ce and In can provoke synergistic effects in reducing the energy gap and stabilizing the structure of the LVO system. The small band gap of the D4 type, with the CBM near the Fermi energy level and very small effective mass, is favorable for the carrier transport and crucial for improving the intrinsic conductivity of LVO.

2.3. Electrochemical Performance. To further clarify the electrochemical modification of 5LICVO/NC, the 2016-type coin cells were assembled for electrochemical testing. Figure 4a shows the first four cycles of cyclic voltammetry (CV) curves of 5LICVO/NC at 0.2 mV s^{-1}. Three reduction peaks located at 0.367, 0.511, and 0.615 Vin the first cycle cathodic scan, reflecting the intercalation of Li^+ into 5LICVO/NC and the formation of the solid electrolyte film (SEI). In contrast, the oxidation peak located at 1.353 V in the first anodic scan reflects the extraction of Li^+. The small potential gap between the reduction with oxidation peaks illustrates the small polarization of the battery. In the subsequent second scan of 5LICVO/NC, the three reduction peaks move toward higher potential and decrease to two reduction peaks at 0.487 and 0.857 V. Simultaneously, the oxidation peak in the first cycle also moves to a lower potential of 1.338 V, which means that the battery achieves activation, and the internal polarization gradually decreased. After the activation, the CV curves from the second to the fourth cycle almost overlapped with each other, indicating good reversibility of the 5LICVO/NC sample. Figure S16a,c represents the first four cycles of CV curves for LCVO/NC and LVO/NC, respectively. It can be found that three reduction peaks at 0.3−0.5, 0.526, and 0.633 V and one oxidation peak at 1.365 V are presented in the first cycle CV of LCVO/NC (the unsmooth curve in the low potential region may originate from the influence of the test environment). Only two reduction peaks at 0.5 and 0.618 V and one oxidation peak at 1.363 V were observed for LVO/NC. The occurrence of a third reduction peak in the low potential region indicates a deeper lithiation of 5LICVO/NC and LCVO/NC, with higher specific capacity and better reaction kinetics.[24] Except for the first cycle, the characteristics of CV curves of three samples were highly similar, indicating that the In/Ce co-doping does not affect the crystalline phase structure of LVO, matching well with the results of XRD analysis.

The galvanostatic discharge/charge curves of 5LICVO/NC for the first three cycles at 0.1 A g^{-1} are presented in Figure 4b. In the first cycle, 5LICVO/NC delivers a discharge capacity of 611.8 mA h g^{-1} and a charge capacity of 418.0 mA h g^{-1}, corresponding to a 68.3% initial coulombic efficiency (ICE). The irreversible capacity loss can be ascribed to two main factors. One aspect is the irreversible intercalation of partial Li^+ into the active material lattice during the first discharge of the electrode, which forms a new phase and leads to the loss of Li^+.[62,63] The other is the further depletion of Li^+ caused by the formation of the SEI, which greatly decreases the ICE.[51] In/ex situ modulation of electrolytes and surface modification are probably effective methods to improve the ICE of this material in subsequent work. The discharge/charge curves of the second and third cycles are well overlapped with each other, indicating the enhanced reversibility of the electrode material. As shown in Figure 4c, when cycled at 0.1 A g^{-1}, the capacity of LVO/NC fades faster than that of the LCVO/NC cell, demonstrating that the Ce doping can stabilize the structure in the bulk phase lattice. 5LICVO/NC has the best cycling stability and specific capacity, maintaining a high discharge capacity of 386.3 mA h g^{-1} after 100 cycles (while the low reversible capacities of 324.6 and 317.8 mA h g^{-1} could be retained for LCVO/NC and LVO/NC, respectively). This displays the outstanding advantages of N-modified carbon-supported In/Ce co-doping for improving the structural stability and cycling performance of LVO. The excellent rate performance of 5LICVO/NC at various current densities is demonstrated in Figure 4d. 5LICVO/NC delivers high capacities (Figure S17a) of 592.0, 377.8, 353.6, 338.1, 324.5, 320.9, 296.2, and 277.9 mA h g^{-1} at 0.05, 0.1, 0.2, 0.4, 0.8, 1.6, 3.2, and 5 A g^{-1}, respectively. These are apparently higher than those of LCVO/NC (Figure S17b, with 582.5, 334.8, 312.5, 294.7, 280.6, 275.1, 259.5, and 248.6 mA h g^{-1}) and LVO/NC (Figure S17c, with 571.8.0, 289.0, 268.3, 250.4, 233.1, 221.5, 193.5, and 169.0 mA h g^{-1}). 5LICVO/NC demonstrates only small capacity fading with rising current densities and still maintains desired capacity at high current densities. This undoubtedly benefits from the strong structural stability and attractive reaction kinetics of the 5LICVO/NC material. When the current density is reset to 0.1 A g^{-1}, the capacity retrieved to 387.0 mA h g^{-1}, illustrating the high reversibility of the electrode (exhibiting a slightly higher capacity than the initial cycles at 0.1 A g^{-1}, possibly due to the electrochemical reconstruction that occurred during the cycle of the 5LICVO/NC[40]).

https://doi.org/10.1021/acsami.2c10471
ACS Appl. Mater. Interfaces 2022, 14, 52702−52714

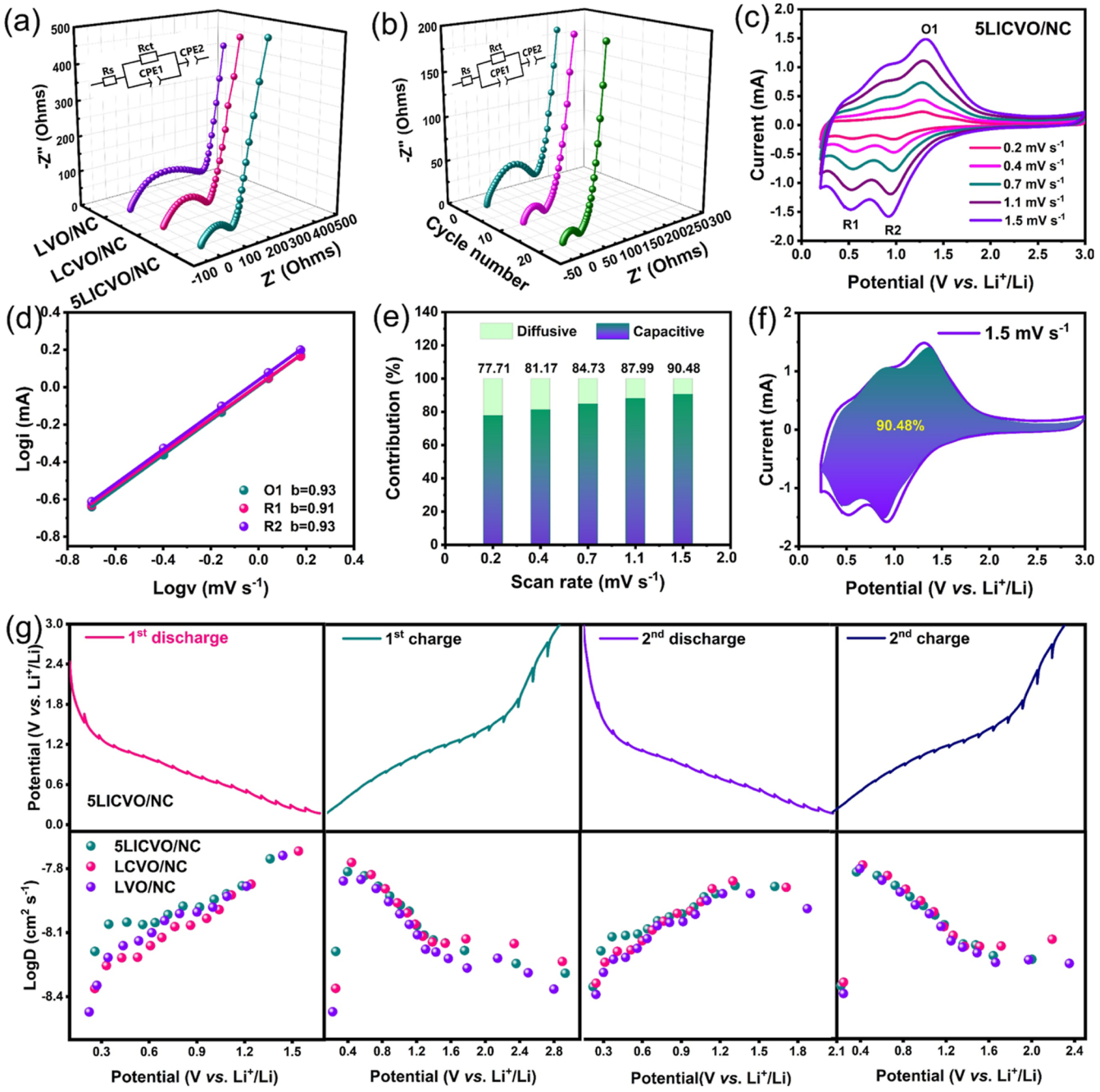

Figure 5. EIS spectra of (a) three samples and (b) fresh, after 10 and 20 cycles at 0.1 A g^{-1} for 5LICVO/NC. (c) CV curves at 0.2−1.5 mV s^{-1} and (d) relationship between the log peak current and log scan rate, (e) capacitive contributions at various scan rates, and (f) 1.5 mV s^{-1} of 5LICVO/NC. (g) GITT images of three samples and the corresponding log *D* point distribution.

Figure 4e represents the long-term cycling performance of three samples at 0.5 A g^{-1} with the first five cycles as the activation processes. A high capacity of 335 mA h g^{-1} can be retained after 1200 cycles for the 5LICVO/NC, corresponding to a high capacity retention of 98.4%. In sharp contrast, the LCVO/NC-based cell can only preserve 285.0 mA h g^{-1} capacity after 1200 cycles (with a capacity retention of 88.0%). For LVO/NC, however, only a low capacity of 235.9 mA h g^{-1} is retained after 1200 cycles, corresponding to only 69.3% retention. In particular, LVO/NC has the lowest discharge capacity (127.6 mA h g^{-1}) at a higher current density of 1.6 A g^{-1} after 2000 cycles (Figure 4f) and more visible capacity fading than that of LCVO/NC and 5LICVO/NC. The inferior electrochemical performance was caused by the poor electrode kinetics and structural stability of LVO/NC. These results also indicate that Ce can stabilize the structure of the bulk phase and improve electrode kinetics. The introduction of In will further enhance the stability of the LVO bulk phase structure and promote the battery reaction kinetics so that 5LICVO/NC can still preserve a high capacity of 259.5 mA h g^{-1} at 1.6 A g^{-1} after 4000 cycles, equal to 78.7% capacity retention (Figure 4f). Although the coulombic efficiency is lost in the initial cycle due to the decomposition of the electrolyte and the formation of SEI, it can consequently maintain nearly 100% in the subsequent cycles, showing the good kinetics of the 5LICVO/NC material. In addition,

https://doi.org/10.1021/acsami.2c10471
ACS Appl. Mater. Interfaces 2022, 14, 52702−52714

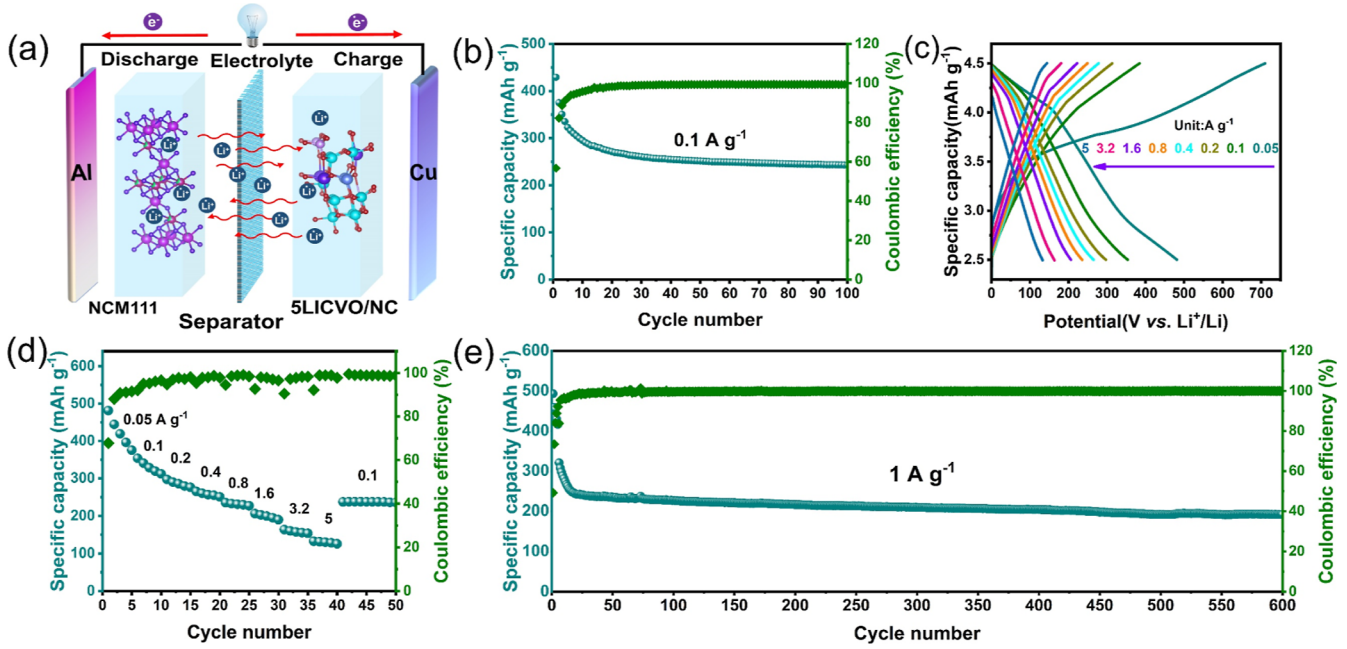

Figure 6. (a) Schematic illustration of the NCM111//5LICVO/NC full cell. (b) Cycling performance at 0.1 A g^{-1}, (c) discharge/charge curves from 0.05 to 5 A g^{-1}, (d) rate performance, and (e) long-term cycling performance at 1 A g^{-1} for the NCM111//5LICVO/NC full cell.

5LICVO/NC exhibits better rate and cycling performance than most previously reported LVO materials (Table S5),[8,9,16,18,20,24,25,43,64−67] demonstrating that the N-modified carbon-supported In/Ce co-doping is a highly efficient modification strategy in this work.

2.4. Reaction Kinetics and Li^+ Intercalation Mechanism. The superior electrochemical performance of 5LICVO/NC can be better appreciated by kinetic analysis. In the Nyquist plots (Figure 5a), the intercept (R_s) at the high-frequency region represents the sum of the electrolyte resistance and ohmic resistance of the battery components, the semicircle mainly reflects the charge transfer resistance (R_{ct}), and the slope in the low-frequency region is mainly related to the Weber diffusion in the electrodes. The impedance spectrum can be better understood by fitting with an equivalent circuit model (Figure 5a inset). In this model, except for R_s and R_{ct}, CPE1 is the constant-phase component related to the double-layer capacitance, while CPE2 is the capacitance related to the accumulation or loss of Li^+ in the electrode.[68] After fitting, the R_{ct} of 5LICVO/NC is 127.4 Ω, which is much smaller than that of LCVO/NC (197.0 Ω) and LVO/NC (323.0 Ω). More importantly, the R_{ct} of 5LICVO/NC is steadily decreasing after 10 and 20 cycles (Figure 5b), reducing to 59.5 and 36.7 Ω, respectively. This benefits from the higher Li^+ diffusion coefficient and electronic conductivity of 5LICVO/NC.

The high ionic diffusion coefficient and electronic conductivity are the keys to excellent rate performance. According to the Randles−Sevchik eq S3, the trend of the Li^+ diffusion coefficient (D) in three samples can be observed from the linear fitting (Figure S18) collected from oxidation peak currents (I_p) versus the square root of the scan rate ($v^{1/2}$) of 5LICVO/NC (Figure 5c), LCVO/NC (Figure S16b), and LVO/NC (Figure S16d). As shown in eq S3, $D^{1/2}$ is proportional to the slope of the fitted curves and steadily becomes bigger from LVO/NC to 5LICVO/NC, corresponding to the above analysis of the above content. D-values can be calculated by the galvanostatic intermittent titration technique (GITT), which can illustrate the effect of multistep intercalation/extraction on ion diffusion and conductivity.[48] Figure 5g represents the GITT curves of three samples during the first two cycles of discharge/charge and the distribution of the calculated log D points (E vs t curves) of the 5LICVO/NC electrode for a single GITT during the discharge process, as shown in Figure S19. The average value of D for 5LICVO/NC is 9.82 × 10^{-9} cm^2 s^{-1}, higher than that of LCVO/NC (9.45 × 10^{-9} cm^2 s^{-1}) and LVO/NC (9.17 × 10^{-9} cm^2 s^{-1}). Four probe tests were conducted to verify that the electronic conductivity of LVO could be improved by doping. The results showed that the electronic conductivity of 5LICVO/NC is 1.38 × 10^{-2} S cm^{-1}, which is remarkably higher than that of LCVO/NC and LVO/NC (7.11 × 10^{-4} and 2.79 × 10^{-4} S cm^{-1}, respectively). LVO/NC has a higher electronic conductivity than that in previous literature.[11,29,32,33,36] This implies that the N-modified conductive carbon nanofibers can provide a good electron transport framework, which emphasizes the superiority of the modification strategy in this work. Simultaneously, the synergistic effect of In/Ce co-doping improved the LVO intrinsic electronic conductivity and enhanced the electrode dynamics.

Superior rate and long-cycling performance are generally dependent on a high electrode capacitive contribution. In the 5LICVO/NC material, the oxygen defects resulting from the V^{4+}/V^{5+} hybrids combined with the extrinsic defects that form the N-modified carbon will provide more active sites to adsorb numerous cations and produce a significant capacitive effect. This can be verified by the following discussion in eqs 1 and 2[46,69]

$$I(\mathrm{V}) = av^b \tag{1}$$

$$I(\mathrm{V}) = k_1 v + k_2 v^{1/2} \tag{2}$$

https://doi.org/10.1021/acsami.2c10471
ACS Appl. Mater. Interfaces 2022, 14, 52702−52714

where v is the scan rate (mV s^{-1}); $I(V)$ is the current (mA) at the corresponding v; a and b are constants; when $0 < b < 0.5$, it indicates that the electrode reaction is mainly controlled by the diffusion behavior, while if $0.5 < b < 1$, it indicates that the electrode reaction is mainly controlled by the capacitive behavior. Figure 5d shows the fitting results collected from $\log(I)$ to $\log(v)$ of the oxidation and reduction peaks (Figure 5c) in 5LICVO/NC at 0.2−1.5 mV s^{-1}. The b-values can be calculated from the slope, and all are close to 1, suggesting that the electrode reaction is mainly controlled by the capacitive behavior. According to eq 2, k_1 (slope) and k_2 (intercept) can be obtained by plotting $I(V)/v^{1/2}$ versus $v^{1/2}$ at different potentials, and the capacitive contribution (k_1v) was calculated, where the results are shown in Figure 5e. The percentage of diffusion in 5LICVO/NC decreases with increasing scan rate, while the contribution of the capacitance gradually increases, reaching 90.48% at 1.5 mV s^{-1} (Figure 5f), which is higher than that of LCVO/NC (90.06%, Figure S20c) and LVO/NC (89.61%, Figure S20f). The high capacitive contribution results from the rich active sites in the 5LICVO/NC nanofibers, which endow the material with superior rate and long-term cycling performance.

2.5. Full-cell Performance. A full cell with Li-$Ni_{1/3}Co_{1/3}Mn_{1/3}O_2$ (NCM111) as the cathode and the 5LICVO/NC anode was assembled to evaluate the potential of 5LICVO/NC to be used as an anode in practical applications (Figure 6a). Pre-lithiation was first carried out in the half-cell for 5LICVO/NC to compensate for the lithium loss in the initial cycle. To ensure the full utilization of the capacity of 5LICVO/NC, the full cell was assembled at a low N/P ratio (a cathode/anode capacity ratio) of 1.2:1 (the range of potential was 2.5−4.5 V). A capacity of 242.6 mA h g^{-1} could be retained after 100 cycles at 0.1 A g^{-1} (Figure 6b) for the NCM111//5LICVO/NC full cell, demonstrating good cycling stability. The discharge capacities of 157.3 and 130.0 mA h g^{-1} could be obtained at high current densities of 3.2 and 5 A g^{-1} (Figure 6c), respectively, and the capacity was reversibly retrieved to 242.6 mA h g^{-1} when reverted to 0.1 A g^{-1} (Figure 6d). Figure 6e shows the long-term cycling performance of the NCM111//5LICVO/NC full cell at 1 A g^{-1} (the first five cycles are the activation processes); a high discharge capacity of 191.9 mA h g^{-1} could be retained after 600 cycles. Despite the slightly lower coulombic efficiency in the initial several cycles caused by the electrolyte decomposition and the SEI formation, it was sustained at about 100% in the successive cycles. The superior rate and cycling performance of the full cell benefit from the favorable structural stability and electrode kinetics of 5LICVO/NC. These merits reveal the potential of 5LICVO/NC for application in the field of battery systems with high energy density and high power density.

3. CONCLUSIONS

In summary, 5LICVO/NC as an anode material for LIBs exhibits superior electrochemical performance, including high reversible specific capacity, excellent rate performance, and long cycle stability. The high discharge capacities of 386.3 and 277.9 mA h g^{-1} could be obtained for 5LICVO/NC at 0.1 and 5 A g^{-1}, respectively. 335 and 259.5 mA h g^{-1} capacities can be maintained after ultra-long cycling of 1200 and 4000 cycles at 0.5 and 1.6 A g^{-1}, corresponding to capacity retention of 98.4 and 78.7%, respectively. The superior electrochemical performance of 5LICVO/NC is ascribed to the synergistic effect generated by In/Ce co-doping, which improves the structural stability of the material, effectively reduces the LVO energy gap, improves the carrier transport capacity, and leads to orders of magnitude increase in the conductivity of LVO (from 2.79×10^{-4} to 1.38×10^{-2} S cm^{-1}). Simultaneously, the good electron transport framework and buffered structural strain benefit from the N−C nanofibers incorporated with LICVO nanoparticles. Thereby, the 5LICVO/NC anode material has great potential application in safe, stable, and high-efficiency LIBs.

■ ASSOCIATED CONTENT

Supporting Information

The Supporting Information is available free of charge at https://pubs.acs.org/doi/10.1021/acsami.2c10471.

Experimental section (material preparation and characterization, electrochemical test, and theoretical calculations); XRD spectra of different In^{3+}/Ce^{4+} molar ratio doped Li_3VO_4; rate performance of 3LICVO/NC and 7LICVO/NC; SEM images of the precursor of 5LICVO/NC nanofibers; Rietveld refined XRD spectra of LCVO/NC and LVO/NC; fractional atomic parameters of 5LICVO/NC; lattice parameters of all samples; FESEM, TEM, and HRTEM images of LCVO/NC and LVO/NC; TG and DTA curves of 5LICVO/NC; high-resolution XPS spectra of LCVO/NC and LVO/NC; crystal structures, calculated energy band structures, and related DOS of mono- and binary-doped Li_3VO_4; UV−vis−NIR spectrum of 5LICVO/NC; CV curves of LCVO/NC and LVO/NC; discharge/charge curves from 0.05 to 5 A g^{-1} of all samples; comparison of electrochemical performances of the Li_3VO_4 material for lithium-ion batteries; relationship between the oxidation peak current and the square root of the scan rate of all samples; E versus t curves of the 5LICVO/NC electrode for a single GITT during the discharge process; and analysis of capacitive contribution in LCVO/NC and LVO/NC electrodes (PDF)

■ AUTHOR INFORMATION

Corresponding Author

Anqiang Pan − *School of Materials Science and Engineering, Key Laboratory of Electronic Packaging and Advanced Functional Materials of Hunan Province, Central South University, Changsha, Hunan 410083, China;* orcid.org/0000-0002-7605-1192; Email: pananqiang@csu.edu.cn

Authors

Yuanlang Wan − *School of Materials Science and Engineering, Key Laboratory of Electronic Packaging and Advanced Functional Materials of Hunan Province, Central South University, Changsha, Hunan 410083, China*

Zhi Chang − *School of Materials Science and Engineering, Key Laboratory of Electronic Packaging and Advanced Functional Materials of Hunan Province, Central South University, Changsha, Hunan 410083, China*

Xuefang Xie − *School of Physical Science and Technology, Xinjiang University, Urumqi 830046, China*

Jialin Li − *School of Physics and Electronics, Key Laboratory of Super Micro-structure and Ultrafast Process of Hunan Province, Central South University, Changsha, Hunan 410083, China;* orcid.org/0000-0003-4598-8326

Simin Chai − *School of Materials Science and Engineering, Key Laboratory of Electronic Packaging and Advanced Functional Materials of Hunan Province, Central South University, Changsha, Hunan 410083, China*
Shuang Zhou − *School of Materials Science and Engineering, Key Laboratory of Electronic Packaging and Advanced Functional Materials of Hunan Province, Central South University, Changsha, Hunan 410083, China*
Qiong He − *School of Materials Science and Engineering, Key Laboratory of Electronic Packaging and Advanced Functional Materials of Hunan Province, Central South University, Changsha, Hunan 410083, China*
Chunyan Fu − *School of Materials Science and Engineering, Key Laboratory of Electronic Packaging and Advanced Functional Materials of Hunan Province, Central South University, Changsha, Hunan 410083, China*
Mingyang Feng − *School of Materials Science and Engineering, Key Laboratory of Electronic Packaging and Advanced Functional Materials of Hunan Province, Central South University, Changsha, Hunan 410083, China*
Guozhong Cao − *Department of Materials Science and Engineering, University of Washington, Seattle, Washington 98195, United States;* orcid.org/0000-0001-6539-0490
Shuquan Liang − *School of Materials Science and Engineering, Key Laboratory of Electronic Packaging and Advanced Functional Materials of Hunan Province, Central South University, Changsha, Hunan 410083, China;* orcid.org/0000-0001-9227-5498

Complete contact information is available at: https://pubs.acs.org/10.1021/acsami.2c10471

Author Contributions

Y.W.: methodology (lead), data curation (lead), validation (lead), and writing (lead). Z.C.: writing-review and editing (lead), project administration (supporting), and resources (supporting). X.X.: project administration (supporting), data curation (supporting), and methodology (supporting). J.L.: investigation (supporting) and data curation (supporting). S.C.: methodology (supporting) and data curation (supporting). S.Z.: methodology (supporting) and data curation (supporting). Q.H.: resources (supporting) and data curation (supporting). C.F.: validation (supporting). M.F.: validation (supporting). G.C.: conceptualization (supporting). S.L.: resources (supporting). A.P.: conceptualization (lead), methodology (equal), resources (lead), writing-review and editing (equal), and project administration (lead). All authors have approved the final version of the manuscript.

Notes

The authors declare no competing financial interest.

■ ACKNOWLEDGMENTS

This work was supported by the National Natural Science Foundation of China (grant no. 51874362, 51932011).

■ REFERENCES

(1) Liu, H.; Zhu, Z.; Yan, Q.; Yu, S.; He, X.; Chen, Y.; Zhang, R.; Ma, L.; Liu, T.; Li, M.; Lin, R.; Chen, Y.; Li, Y.; Xing, X.; Choi, Y.; Gao, L.; Cho, H. S.; An, K.; Feng, J.; Kostecki, R.; Amine, K.; Wu, T.; Lu, J.; Xin, H. L.; Ong, S. P.; Liu, P. A Disordered Rock Salt Anode for Fast-Charging Lithium-Ion Batteries. *Nature* **2020**, *585*, 63−67.
(2) He, Q.; Fang, G.; Chang, Z.; Zhang, Y.; Zhou, S.; Zhou, M.; Chai, S.; Zhong, Y.; Cao, G.; Liang, S.; Pan, A. Building Ultra-Stable and Low-Polarization Composite Zn Anode Interface Via Hydrated Polyzwitterionic Electrolyte Construction. *Nano-Micro Lett.* **2022**, *14*, 93.
(3) Liu, Y.; Li, W.; Xia, Y. Y. Recent Progress in Polyanionic Anode Materials for Li (Na)-Ion Batteries. *Electrochem. Energy Rev.* **2021**, *4*, 447−472.
(4) Wu, F.; Liu, M. Q.; Li, Y.; Feng, X.; Zhang, K.; Bai, Y.; Wang, X. R.; Wu, C. High-Mass-Loading Electrodes for Advanced Secondary Batteries and Supercapacitors. *Electrochem. Energy Rev.* **2021**, *4*, 382−446.
(5) Li, H.; Liu, X.; Zhai, T.; Li, D.; Zhou, H. Li3VO4: A Promising Insertion Anode Material for Lithium-Ion Batteries. *Adv. Energy Mater.* **2013**, *3*, 428−432.
(6) Xu, X. M.; Xiong, F. Y.; Meng, J. S.; Wang, X. P.; Niu, C. J.; An, Q. Y.; Mai, L. Q. Vanadium-Based Nanomaterials: A Promising Family for Emerging Metal-Ion Batteries. *Adv. Funct. Mater.* **2020**, *30*, 1904398.
(7) Liang, Z.; Lin, Z.; Zhao, Y.; Dong, Y.; Kuang, Q.; Lin, X.; Liu, X.; Yan, D. New understanding of Li3VO4/C as potential anode for Li-ion batteries: Preparation, structure characterization and lithium insertion mechanism. *J. Power Sources* **2015**, *274*, 345−354.
(8) Shao, G.; Gan, L.; Ma, Y.; Li, H.; Zhai, T. Enhancing the performance of Li3VO4 by combining nanotechnology and surface carbon coating for lithium ion batteries. *J. Mater. Chem. A* **2015**, *3*, 11253−11260.
(9) Sun, Y.; Li, C. S.; Yang, C.; Dai, G. L.; Li, L.; Hu, Z.; Wang, D. D.; Liang, Y. R.; Li, Y. L.; Wang, Y. X.; Xu, Y. F.; Zhao, Y. Z.; Liu, H. K.; Chou, S. L.; Zhu, Z.; Wang, M. M.; Zhu, J. H. Novel Li 3 VO 4 Nanostructures Grown in Highly Efficient Microwave Irradiation Strategy and Their In-Situ Lithium Storage Mechanism. *Adv. Sci.* **2022**, *9*, 2103493.
(10) Arroyo-de Dompablo, M. E.; Tartaj, P.; Amarilla, J. M.; Amador, U. Computational Investigation of Li Insertion in Li3VO4. *Chem. Mater.* **2016**, *28*, 5643−5651.
(11) Zhao, L.; Duan, H.; Zhao, Y.; Kuang, Q.; Fan, Q.; Chen, L.; Dong, Y. High capacity and stability of Nb-doped Li3VO4 as an anode material for lithium ion batteries. *J. Power Sources* **2018**, *378*, 618−627.
(12) Shen, L. F.; Chen, S. Q.; Maier, J.; Yu, Y. Carbon-Coated Li3 VO4 Spheres as Constituents of an Advanced Anode Material for High-Rate Long-Life Lithium-Ion Batteries. *Adv. Mater.* **2017**, *29*, 1701571.
(13) Zhang, C.; Liu, C.; Nan, X.; Song, H.; Liu, Y.; Zhang, C.; Cao, G. Hollow-Cuboid Li3VO4/C as High-Performance Anodes for Lithium-Ion Batteries. *ACS Appl. Mater. Interfaces* **2016**, *8*, 680−688.
(14) Yang, Y.; Li, J.; Huang, J.; Huang, J.; Zeng, J.; Zhao, J. Polystyrene-template-assisted synthesis of Li3VO4/C/rGO ternary composite with honeycomb-like structure for durable high-rate lithium ion battery anode materials. *Electrochim. Acta* **2017**, *247*, 771−778.
(15) Qin, P.; Lv, X.; Li, C.; Zheng, Y.-Z.; Tao, X. Morphology inheritance synthesis of carbon-coated Li3VO4 rods as anode for lithium-ion battery. *Sci. China Mater.* **2019**, *62*, 1105−1114.
(16) Qin, R.; Shao, G.; Hou, J.; Zheng, Z.; Zhai, T.; Li, H. One-pot synthesis of Li3VO4@C nanofibers by electrospinning with enhanced electrochemical performance for lithium-ion batteries. *Sci. Bull.* **2017**, *62*, 1081−1088.
(17) Xu, Z.; Li, D. B.; Xu, J.; Lu, J. L.; Zhang, D. M.; Ni, S. B. Controllable synthesis of Li3VO4/N doped C nanofibers toward high-capacity and high-rate Li-ion storage. *Electrochim. Acta* **2021**, *384*, 138386.
(18) Ni, S.; Lv, X.; Zhang, J.; Ma, J.; Yang, X.; Zhang, L. The electrochemical performance of lithium vanadate/natural graphite composite material as anode for lithium ion batteries. *Electrochim. Acta* **2014**, *145*, 327−334.
(19) Jin, X.; Lei, B.; Wang, J.; Chen, Z.; Xie, K.; Wu, F.; Song, Y.; Sun, D.; Fang, F. Pomegranate-like Li 3 VO 4 /3D graphene networks nanocomposite as lithium ion battery anode with long cycle life and high-rate capability. *J. Alloys Compd.* **2016**, *686*, 227−234.

(20) Xu, X.; Niu, F.; Zhang, D.; Chu, C.; Wang, C.; Yang, J.; Qian, Y. Hierarchically porous Li3VO4/C nanocomposite as an advanced anode material for high-performance lithium-ion capacitors. *J. Power Sources* **2018**, *384*, 240−248.
(21) Xu, X.; Niu, F.; Wang, C.; Li, Y.; Zhao, C.; Yang, J.; Qian, Y. Li3VO4 nanoparticles in N-doped carbon with porous structure as an advanced anode material for lithium-ion batteries. *Chem. Eng. J.* **2019**, *370*, 606−613.
(22) Ren, X. L.; Ai, D. S.; Zhan, C. Z.; Lv, R. T.; Kang, F. Y.; Huang, Z. H. 3D porous Li3VO4@C composite anodes with ultra-high rate capacity for lithium-ion capacitors. *Electrochim. Acta* **2020**, *355*, 136819.
(23) Yang, Y.; Li, J.; Chen, D.; Zhao, J. Spray Drying-Assisted Synthesis of Li3VO4/C/CNTs Composites for High-Performance Lithium Ion Battery Anodes. *J. Electrochem. Soc.* **2016**, *164*, A6001−A6006.
(24) Huang, Y. H.; Yang, H. C.; Zhang, Y.; Zhang, Y. M.; Wu, Y. T.; Tian, M. K.; Chen, P.; Trout, R.; Ma, Y.; Wu, T. H.; Wu, Y. P.; Liu, N. A safe and fast-charging lithium-ion battery anode using MXene supported Li3VO4. *J. Mater. Chem. A* **2019**, *7*, 11250−11256.
(25) Ni, S.; Lv, X.; Ma, J.; Yang, X.; Zhang, L. The fabrication of Li3VO4/Ni composite material and its electrochemical performance as anode for Li-ion battery. *Electrochim. Acta* **2014**, *130*, 800−804.
(26) Zhou, J.; Zhao, B.; Song, J.; Chen, B.; Bai, J.; Fang, Z.; Dai, J.; Zhu, X.; Sun, Y. Three-Dimensional Porous Hierarchically Architectured Li3VO4 Anode Materials for High-Performance Lithium-Ion Batteries. *ACS Appl. Energy Mater.* **2018**, *2*, 354−362.
(27) Liao, C.; Zhang, Q.; Zhai, T.; Li, H.; Zhou, H. Development and perspective of the insertion anode Li 3 VO 4 for lithium-ion batteries. *Energy Storage Mater.* **2017**, *7*, 17−31.
(28) Liu, X.; Li, G.; Zhang, D.; Chen, D.; Wang, X.; Li, B.; Li, L. Fe-doped Li3VO4 as an excellent anode material for lithium ion batteries: Optimizing rate capability and cycling stability. *Electrochim. Acta* **2019**, *308*, 185−194.
(29) Dong, Y.; Duan, H.; Park, K. S.; Zhao, Y. Mo6+ Doping in Li3VO4 Anode for Li-Ion Batteries: Significantly Improve the Reversible Capacity and Rate Performance. *ACS Appl. Mater. Interfaces* **2017**, *9*, 27688−27696.
(30) Chung, S. Y.; Bloking, J. T.; Chiang, Y. M. Electronically Conductive Phospho-Olivines as Lithium Storage Electrodes. *Nat. Mater.* **2002**, *1*, 123−128.
(31) Shan, H.; Qin, J.; Wang, J. J.; Sari, H. M. K.; Lei, L.; Xiao, W.; Li, W. B.; Xie, C.; Yang, H. J.; Luo, Y. Y.; Zhang, G. N.; Li, X. F. Doping-Induced Electronic/Ionic Engineering to Optimize the Redox Kinetics for Potassium Storage: A Case Study of Ni-Doped CoSe 2. *Adv. Sci.* **2022**, *9*, 2200341.
(32) Liang, G. S.; Yang, L. T.; Han, Q.; Chen, G. Y.; Lin, C. F.; Chen, Y. J.; Luo, L. J.; Liu, X. H.; Li, Y. S.; Che, R. C. Conductive Li 3.08 Cr 0.02 Si 0.09 V 0.9 O 4 Anode Material: Novel "Zero-Strain" Characteristic and Superior Electrochemical Li + Storage. *Adv. Energy Mater.* **2020**, *10*, 1904267.
(33) Huu, H. T.; Vu, N. H.; Ha, H.; Moon, J.; Kim, H. Y.; Im, W. B. Sub-micro droplet reactors for green synthesis of Li3VO4 anode materials in lithium ion batteries. *Nat. Commun.* **2021**, *12*, 3081.
(34) Wang, K.; Fu, H. Y.; Li, Z. Y.; Xia, M. Y.; Liang, X. Q.; Qi, R. J.; Cao, G. Z.; Lu, X. M. Enhancing the Rate Performance of a Li3 VO4 Anode through Cu Doping. *ChemElectroChem* **2018**, *5*, 478−482.
(35) Zhang, C.; Wang, K.; Liu, C.; Nan, X.; Fu, H.; Ma, W.; Li, Z.; Cao, G. Effects of high surface energy on lithium-ion intercalation properties of Ni-doped Li3VO4. *NPG Asia Mater.* **2016**, *8*, No. e287.
(36) Dong, Y.; Zhao, Y.; Duan, H.; Singh, P.; Kuang, Q.; Peng, H. Li2.97Mg0.03VO4: High rate capability and cyclability performances anode material for rechargeable Li-ion batteries. *J. Power Sources* **2016**, *319*, 104−110.
(37) Mu, C.; Lei, K.; Li, H.; Li, F.; Chen, J. Enhanced Conductivity and Structure Stability of Ti4+ Doped Li3VO4 as Anodes for Lithium-Ion Batteries. *J. Phys. Chem. C* **2017**, *121*, 26196−26201.
(38) Chi, X.; Zhang, J.; Wen, Z.; Liu, Y.; Wu, M.; Wu, X. Influence of In doping on the structure, stability and electrical conduction behavior of Ba(Ce,Ti)O3 solid solution. *J. Alloys Compd.* **2013**, *554*, 378−384.
(39) Sreerung, R.; Raknual, D.; Vailikhit, V.; Teesetsopon, P.; Kitisripanya, N.; Tubtimtae, A. Structural and electrochemical studies of undoped and In3+-doped co-binary Cu2-xTe and Bi2Te3 thin films for aqueous Na-S batteries. *Ceram. Int.* **2019**, *45*, 17305−17317.
(40) Ni, S. B.; Zhang, J. C.; Ma, J. J.; Yang, X. L.; Zhang, L. L.; Li, X. M.; Zeng, H. B. Approaching the Theoretical Capacity of Li3VO4via Electrochemical Reconstruction. *Adv. Mater. Interfac.* **2016**, *3*, 1500340.
(41) Zhang, C.; Song, H.; Liu, C.; Liu, Y.; Zhang, C.; Nan, X.; Cao, G. Fast and Reversible Li Ion Insertion in Carbon-Encapsulated Li3VO4as Anode for Lithium-Ion Battery. *Adv. Funct. Mater.* **2015**, *25*, 3497−3504.
(42) Yang, Z. H.; Li, W. B.; Zhang, G. N.; Wang, J. J.; Zuo, J. X.; Xu, Q.; Shan, H.; He, X. F.; Lv, M. F.; Hu, J. H.; Huang, W.; Zhang, J. J.; Li, X. F. Constructing Sb O C bond to improve the alloying reaction reversibility of free-standing Sb2Se3 nanorods for potassium-ion batteries. *Nano Energy* **2022**, *93*, 106764.
(43) Chen, L.; Jiang, X. L.; Wang, N. N.; Yue, J.; Qian, Y. T.; Yang, J. Surface-Amorphous and Oxygen-Deficient Li3VO4−δas a Promising Anode Material for Lithium-Ion Batteries. *Adv. Sci.* **2015**, *2*, 1500090.
(44) Xia, M. T.; Chen, B. J.; Gu, F.; Zu, L. H.; Xu, M. Z.; Feng, Y. T.; Wang, Z. J.; Zhang, H. J.; Zhang, C.; Yang, J. H. Ti3C2Tx MXene Nanosheets as a Robust and Conductive Tight on Si Anodes Significantly Enhance Electrochemical Lithium Storage Performance. *ACS Nano* **2020**, *14*, 5111−5120.
(45) Zhao, R. Z.; Di, H. X.; Hui, X. B.; Zhao, D. Y.; Wang, R. T.; Wang, C. X.; Yin, L. W. Self-assembled Ti3C2 MXene and N-rich porous carbon hybrids as superior anodes for high-performance potassium-ion batteries. *Energy Environ. Sci.* **2020**, *13*, 246−257.
(46) Xie, X.; Hu, Y.; Fang, G.; Cao, X.; Yin, B.; Wang, Y.; Liang, S.; Cao, G.; Pan, A. Towards a durable high performance anode material for lithium storage: stabilizing N-doped carbon encapsulated FeS nanosheets with amorphous TiO2. *J. Mater. Chem. A* **2019**, *7*, 16541−16552.
(47) Guo, Q. B.; Ma, Y. F.; Chen, T. T.; Xia, Q. Y.; Yang, M.; Xia, H.; Yu, Y. Cobalt Sulfide Quantum Dot Embedded N/S-Doped Carbon Nanosheets with Superior Reversibility and Rate Capability for Sodium-Ion Batteries. *ACS Nano* **2017**, *11*, 12658−12667.
(48) Yin, B.; Cao, X. X.; Pan, A. Q.; Luo, Z. G.; Dinesh, S.; Lin, J. D.; Tang, Y.; Liang, S. Q.; Cao, G. Z. Encapsulation of CoS x Nanocrystals into N/S Co-Doped Honeycomb-Like 3D Porous Carbon for High-Performance Lithium Storage. *Adv. Sci.* **2018**, *5*, 1800829.
(49) Shen, L. F.; Lv, H. F.; Chen, S. Q.; Kopold, P.; van Aken, P. A.; Wu, X. J.; Maier, J.; Yu, Y. Peapod-like Li3 VO4 /N-Doped Carbon Nanowires with Pseudocapacitive Properties as Advanced Materials for High-Energy Lithium-Ion Capacitors. *Adv. Mater.* **2017**, *29*, 1700142.
(50) Lim, S.; Yoon, S. H.; Mochida, I.; Jung, D. H. Direct Synthesis and Structural Analysis of Nitrogen-Doped Carbon Nanofibers. *Langmuir* **2009**, *25*, 8268.
(51) Liu, H.; Hu, P.; Yu, Q.; Liu, Z.; Zhu, T.; Luo, W.; Zhou, L.; Mai, L. Boosting the Deep Discharging/Charging Lithium Storage Performances of Li3VO4 through Double-Carbon Decoration. *ACS Appl. Mater. Interfaces* **2018**, *10*, 23938−23944.
(52) Xu, J.; Liang, P.; Zhang, D.; Pei, C.; Zhang, Z.; Yang, S.; Ni, S. A reverse-design-strategy for C@Li3VO4 nanoflakes toward superb high-rate Li-ion storage. *J. Mater. Chem. A* **2021**, *9*, 17270−17280.
(53) Yang, S. Y.; Xu, Z.; Xu, J.; Lu, J. L.; Zhang, D. M.; Ni, S. B. High capacity Li3VO4-Ga2O3/NC as durable anode for Li-ion batteries via robust pseudocapacitive charge storage. *J. Alloys Compd.* **2021**, *868*, 159115.
(54) Yang, S. Y.; Zhang, D. M.; Xu, J.; Zhang, Z. P.; Ni, S. B. Robust pseudocapacitive charge storage behavior in Li3VO4 induced by N doped MXene. *Electrochim. Acta* **2021**, *388*, 138567.
(55) Kumar Mohanta, M.; Kanta Sahu, T.; Alam, S.; Qureshi, M. Tuning the Electronic Structure of Monoclinic Tungsten Oxide

Nanoblocks by Indium Doping for Boosted Photoelectrochemical Performance. *Chem.—Asian J.* **2020**, *15*, 3886−3896.
(56) Lei, Y. Q.; Song, S. Y.; Fan, W. Q.; Xing, Y.; Zhang, H. J. Facile Synthesis and Assemblies of Flowerlike SnS2 and In3+-Doped SnS2: Hierarchical Structures and Their Enhanced Photocatalytic Property. *J. Phys. Chem. C* **2009**, *113*, 1280−1285.
(57) Li, J.; Zhao, G.; Zhao, H.; Zhao, N.; Lu, L.; Liu, N.; Wang, M.; Ma, C.; Zhang, Q.; Du, Y. Cerium-Doped Bimetal Organic Framework as a Superhigh Capacity Cathode for Rechargeable Alkaline Batteries. *Nanoscale* **2021**, *13*, 3581−3587.
(58) Han, X. Y.; Cui, Y. P.; Liu, H. W. Ce-doped Mn3O4 as high-performance anode material for lithium ion batteries. *J. Alloys Compd.* **2020**, *814*, 152348.
(59) Fan, H. T.; Jin, Y. J.; Liu, K. C.; Liu, W. S. One-Step MOF-Templated Strategy to Fabrication of Ce-Doped ZnIn 2 S 4 Tetrakaidecahedron Hollow Nanocages as an Efficient Photocatalyst for Hydrogen Evolution. *Adv. Sci.* **2022**, *9*, 2104579.
(60) Nguyen, C. Q.; Ang, Y. S.; Nguyen, S. T.; Hoang, N. V.; Hung, N. M.; Nguyen, C. V. Tunable type-II band alignment and electronic structure of C3N4/MoSi2N4 heterostructure: Interlayer coupling and electric field. *Phys. Rev. B* **2022**, *105*, 045303.
(61) Bafekry, A.; Faraji, M.; Hieu, N. N.; Ang, Y. S.; Karbasizadeh, S.; Abdolhosseini Sarsari, I. A.; Ghergherehchi, M. Two-dimensional Dirac half-metal in porous carbon nitride C6N7 monolayer via atomic doping. *Nanotechnology* **2022**, *33*, 075707.
(62) Zhou, L. L.; Shen, S. Y.; Peng, X. X.; Wu, L. N.; Wang, Q.; Shen, C. H.; Tu, T. T.; Huang, L.; Li, J. T.; Sun, S. G. New Insights into the Structure Changes and Interface Properties of Li3VO4 Anode for Lithium-Ion Batteries during the Initial Cycle by in-Situ Techniques. *ACS Appl. Mater. Interfaces* **2016**, *8*, 23739−23745.
(63) Asakura, R.; Bolli, C.; Novák, P.; Robert, R. Insights into the Charge Storage Mechanism of Li 3 VO 4 Anode Materials for Li-Ion Batteries. *ChemElectroChem* **2020**, *7*, 2033−2041.
(64) Zhang, M. X.; Dong, L.; Zhang, C. W.; Yin, F. X.; Peng, H. F.; Wang, G. K. Heterogeneous nucleation of Li3VO4 regulated in dense graphene aerogel for lithium ion capacitors. *J. Power Sources* **2020**, *468*, 228364.
(65) Jian, Z. L.; Zheng, M. B.; Liang, Y. L.; Zhang, X. X.; Gheytani, S.; Lan, Y. C.; Shi, Y.; Yao, Y. Li3VO4 anchored graphene nanosheets for long-life and high-rate lithium-ion batteries. *Chem. Commun.* **2015**, *51*, 229−231.
(66) Yang, C.; Ran, Y.; Gao, C.; Wang, Z.; Ding, Y.-L. Hierarchical hybrid architectures assembled from carbon coated Li3VO4 and in-situ generated N-doped graphene framework towards superior lithium storage. *J. Alloys Compd.* **2022**, *918*, 165668.
(67) Deng, J. B.; Lv, C. P.; Jiang, T.; Ma, S. Y.; Liu, X. H.; Lin, C. F. Selective Doping to Controllably Tailor Maximum Unit-Cell-Volume Change of Intercalating Li + -Storage Materials: A Case Study of γ Phase Li 3 VO 4. *Adv. Sci.* **2022**, 202106003.
(68) Li, S.; Qu, Z.; Luo, S.; Guo, Y.; Wan, Z.; Kong, X. Encapsulated Li 3 VO 4 /Carbon with a Continuous Conductive Carbon Framework as an Anode for High-Performance Lithium-Ion Batteries. *ChemElectroChem* **2020**, *7*, 3984−3990.
(69) Shan, H.; Qin, J.; Ding, Y. C.; Sari, H. M. K.; Song, X. X.; Liu, W.; Hao, Y. C.; Wang, J. J.; Xie, C.; Zhang, J. J.; Li, X. F. Controllable Heterojunctions with a Semicoherent Phase Boundary Boosting the Potassium Storage of CoSe 2 /FeSe 2. *Adv. Mater.* **2021**, *33*, 2102471.

https://doi.org/10.1021/acsami.2c10471
ACS Appl. Mater. Interfaces 2022, 14, 52702−52714